Conditional quantum dynamics and nonlocal states in dimeric and trimeric arrays of organic molecules

Reina, John H.; Susa, Cristian E.; Hildner, Richard

Published in:
Physical Review A

DOI:
10.1103/PhysRevA.97.063422

Publication date:
2018

Conditional quantum nonlocality in dimeric and trimeric arrays of organic molecules

John H. Reina,[1,2,*] Cristian E. Susa,[1,3,†] and Richard Hildner[4]

[1] *Centre for Bioinformatics and Photonics—CIBioFi, Calle 13 No. 100-00, Edificio 320 No. 1069, Universidad del Valle, 760032 Cali, Colombia*

[2] *Departamento de Física, Universidad del Valle, 760032 Cali, Colombia*

[3] *Departamento de Física y Electrónica, Universidad de Córdoba, 230002 Montería, Colombia*

[4] *Soft Matter Spectroscopy, Universität Bayreuth, Universitätsstrasse 30, 95447 Bayreuth, Germany*

Arrays of covalently bound organic molecules possess potential for light-harvesting and energy transfer applications due to the strong coherent dipole-dipole coupling between the transition dipole moments of the molecules involved. Here, we show that such molecular systems, based on perylene-molecules, can be considered as arrays of qubits that are amenable for laser-driven quantum coherent control. The perylene monomers exhibit dephasing times longer than four orders of magnitude a typical gating time, thus allowing for the execution of a large number of gate operations on the sub-picosecond timescale. Specifically, we demonstrate quantum logic gates and entanglement in bipartite (dimer) and tripartite (trimer) systems of perylene-based arrays. In dimers, naturally entangled states with a tailored degree of entanglement can be produced. The nonlocality of the molecular trimer entanglement is demonstrated by testing Mermin's (Bell-like) inequality violation.

I. INTRODUCTION

Quantum coherence has been identified as an emergent resource [1–7] for biological and chemical functionality [2, 6]. Understanding and, particularly, exploiting these features on a molecular level has become feasible in recent years through the progress in spectroscopy and quantum control of single molecular systems [8–12]. Recent evidence points out that quantum coherence can be robust and survive even at ambient conditions [1, 2, 4–7, 13–15], a fact that can be harnessed for engineering and transferring quantum information in a wide variety of organic nanosystems: Multichromophoric and biomolecular structures for light harvesting [5–7, 13–17], as well as complex chemical structures for organic photovoltaics with relevance to sustainable renewable energy production [2, 4, 13, 18]. An important advantage of organic systems is that these materials can be easily scaled up by chemical synthesis [1, 4, 18], and do not require complex settings like high-vacuum traps for their implementation [4, 13, 18].

Here, we show that, thanks to the recent advances in single-molecule spectroscopy, we are able to manipulate and to individually control molecular dynamics on the picosecond and sub-picosecond time scales, i.e., we can generate a conditional coherent quantum dynamics and robust entanglement in Perylene-Bisimide (PBI) based arrays immersed in an organic matrix. We specifically focus on such polycyclic aromatic hydrocarbon based molecules, because they can be easily synthesised and can be externally driven with a high degree of control [9, 12, 17, 19, 20].

This paper is organised as follows: In section II, we briefly introduce the physical properties of the PBI dimer and trimer according to spectroscopy data. Section III describes the theory behind the temporal evolution of dimer and trimer states. Dimer's structure for implementing quantum logic gates and entanglement is shown in Section IV. We describe entanglement generation and quantum nonlocality in trimers in Section V. Finally, a summary of our findings and experimental remarks for a physical implementation are discussed in Section VI.

II. SPECTROSCOPY OF MOLECULAR DIMERS AND TRIMERS: DEFINING MOLECULAR QUBIT REGISTERS

As building blocks for quantum information processing units we consider here a molecular array consisting of two (three) PBI molecules that are covalently linked by a rigid calix[4]arene bridge [17, 21].

* john.reina@correounivalle.edu.co

† cristiansusa@correo.unicordoba.edu.co

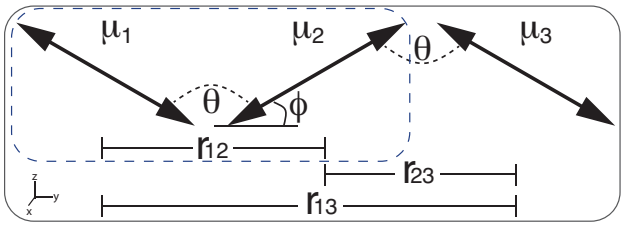

FIG. 1. Schematics of the mutual orientations of the transition dipole moments (double-headed arrows) of covalently bound PBI molecules in trimer (black-solid box) and dimer arrangement (blue-dashed box). $\boldsymbol{\mu}_i$ corresponds to the transition dipole moment of the i-th PBI molecule. θ is the angle between subunits 1 and 2 (also 2 and 3). Subunits 1 and 3 are parallel to each other. The separation vectors between PBI molecules are $|\boldsymbol{r}_{12}| = |\boldsymbol{r}_{23}| = |\boldsymbol{r}_{13}|/2$.

In the following those arrays will be referred to as dimers (trimers). We specifically focus on those PBI systems because we characterised their photophysics extensively by single-molecule techniques [17, 19–21]; moreover, PBIs are very bright and photostable. Considering for each PBI molecule only the lowest-energy optical transition, i.e., the transition between the electronic ground state ($|g\rangle$) and the vibrationless lowest-energy excited state ($|e\rangle$), each PBI in a dimer (trimer) represents a two-state (qubit) system, with basis states $|g_i\rangle \equiv |0_i\rangle$ and $|e_i\rangle \equiv |1_i\rangle$. Thus, in what follows, $\{|0_i\rangle, |1_i\rangle\}$ denotes the computational basis associated to qubit i-th.

The transition dipole moment $\boldsymbol{\mu}_i$ $(i = 1, 2, 3)$ for this lowest-energy transition is oriented along the long axis of PBI. Owing to the rigid bridge the zig-zag-type arrangement for the transition dipole moments shown in Fig. 1 results for a dimer (trimer), with a centre-to-centre distance of $|\boldsymbol{r}_{12}| = |\boldsymbol{r}_{23}| = 2.2$ nm and an opening angle $\theta = 2\pi/3$.

For the specific quantum control experiments proposed here we consider dimers and trimers embedded in a well-defined, crystalline matrix at cryogenic temperature (1.5 K). Under these conditions we found that the lowest-energy optical transition in PBI molecules occurs at a photon frequency of $\nu_i \sim 522$ THz, corresponding to a wavelength of $\lambda_i = 575$ nm [19, 20]. Moreover, in this situation the homogeneous line width of the PBI molecules [8], $\gamma_h = 1/(2\pi T_1) + 1/(\pi T_2^*)$, is entirely determined by its excited state lifetime T_1, because pure dephasing processes, described by the time constant T_2^*, are frozen out ($T_2^* \to \infty$). For PBI molecules we measured $T_1 = 5.8$ ns [19], and thus we obtain $\gamma_h \sim 27$ MHz.

A further fundamental physical parameter for our dimer and trimer systems is the nearest-neighbour electronic coupling $V_{ij} (i \neq j)$ between the transition dipole moments of the individual PBI molecules. Given the magnitude of the transition dipole moment $|\boldsymbol{\mu}_i| = 10$ D [19, 21] and the relatively small centre-to-centre distance, an electronic coupling of ~ 1356 GHz (or 45 cm^{-1}) between adjacent PBIs can be calculated (see Appendix A).

An important figure of merit for performing quantum gates on a dimer (trimer) is the ratio between the nearest-neighbour electronic coupling V_{ij} and the molecular detuning, which is defined as $\Delta_{ij} := \nu_i - \nu_j$. Previously, we considered a ratio of $V_{ij}/\Delta_{ij} \sim 0.1$ as typical for performing dimeric conditional quantum dynamics [22]. However, we found experimentally that the difference in transition frequencies Δ_{ij} can assume any value between 0 and 570 cm^{-1} (17 THz) depending on the specific local environment for each PBI molecule in a dimer (trimer) [17, 20], even if embedded in a well-defined matrix at low temperatures. This means that the ratio V_{ij}/Δ_{ij} can run from very large ($\gg 1$) to small ($\ll 1$), depending on the specific dimer (trimer) under investigation. As we cannot control this detuning experimentally, we perform initial calculations for some exemplary values in the entire range ($\gg 1$ to $\ll 1$). Then we will proceed to identify which effects are to be expected and what to look for in the experiments. Since both V_{ij} and Δ_{ij} are much smaller than the transition frequencies of the PBI molecules, the rotating wave approximation (RWA) is well suited for describing the dimers' and trimers' quantum dynamics [22, 23].

III. DIMER AND TRIMER DISSIPATIVE QUANTUM DYNAMICS

For the mathematical description of the quantum dynamics of PBI dimers and trimers we follow the description given in [22–27]. For the dimer, the effective Hamiltonian after making the standard Born-Markov approximation on the system-environment interaction [23, 26, 27], can be written as ($h = 1$),

$$H_{\text{dimer}} = H_Q + H_{12}, \tag{1}$$

where $H_Q = -\frac{1}{2}(\nu_1 \sigma_z^{(1)} + \nu_2 \sigma_z^{(2)})$, and $H_{12} = \frac{1}{2} V_{12} (\sigma_x^{(1)} \otimes \sigma_x^{(2)} + \sigma_y^{(1)} \otimes \sigma_y^{(2)})$.

The matrix representation of $H_{\rm dimer}$ in the computational basis of product states $|i_1\rangle \otimes |j_2\rangle$ $(i,j=0,1)$ reads

$$H_{\rm dimer} = \begin{pmatrix} -\nu_0 & 0 & 0 & 0 \\ 0 & -\frac{\Delta_-}{2} & V_{12} & 0 \\ 0 & V_{12} & \frac{\Delta_-}{2} & 0 \\ 0 & 0 & 0 & \nu_0 \end{pmatrix}, \qquad (2)$$

where the molecular detuning is $\Delta_- := \Delta_{12} = \nu_1 - \nu_2$, and $2\nu_0 = \nu_1 + \nu_2$.

An external control can be included to the dynamics by means of the light-matter Hamiltonian $H_L = \Omega_i/2(\sigma_-^{(i)} e^{{\rm i}\omega_L t} + \sigma_+^{(i)} e^{-{\rm i}\omega_L t})$ [22, 23, 26], $\omega_L = 2\pi\nu_L$, where ν_L denotes the laser frequency, and $\Omega_i = -\boldsymbol{\mu}_i \cdot \boldsymbol{E}_i$ gives the Rabi frequency induced by the interaction between the i-th transition dipole moment $\boldsymbol{\mu}_i$ and the coherently driving electric field $\boldsymbol{E}_i$ acting on qubit i located at position $\boldsymbol{r}_i$. $\sigma_+^{(i)} = |1_i\rangle\langle 0_i|$ and $\sigma_-^{(i)} = |0_i\rangle\langle 1_i|$ stand for the raising and lowering operators, respectively. Due to the short separation between qubits compared to the optical diffraction limit, we consider that the laser affects both qubits in the same way. Hence, in our simulations we fix $\Omega_1 = \Omega_2 = \Omega$.

Since we consider here cryogenic temperatures, we can assume a zero-temperature environment. Within the weak light-matter interaction (Born-Markov) approximation, the time evolution of the density matrix operator associated to the qubit-qubit system can then be approached by means of the quantum master equation [22, 27]

$$\dot{\rho} = -{\rm i}[\tilde{H}_{\rm dimer}, \rho] - \frac{1}{2}\sum_{i,j=1}^{2} \Gamma_{ij}\Big(\rho\sigma_+^{(i)}\sigma_-^{(j)} + \sigma_+^{(i)}\sigma_-^{(j)}\rho - 2\sigma_-^{(j)}\rho\sigma_+^{(i)}\Big), \qquad (3)$$

where $\tilde{H}_{\rm dimer} = H_{\rm dimer} + H_L$. The density matrix elements are denoted by $\rho_{ij,kl}$, with $i,j,k,l = 0,1$. $\Gamma_{ii} \equiv \Gamma$ are the spontaneous emission rates, and $\Gamma_{ij}, i \neq j$, represent cross-damping rates, for which the explicit forms are given in appendix A. Given the PBI excited state lifetime of $T_1 \sim 5.8$ ns, we get $\Gamma_i = 1/T_1 \sim 172$ MHz. Based on Eq. (A1) we estimate the cross-damping rate to $\Gamma_{12} \sim -86$ MHz.

For the trimer we are able to derive analytical expressions for the three-qubit eigensystem by considering that qubit 1 and qubit 3 (the 'outer' PBI molecules, see Fig. 1) have the same transition frequency ν. Hence, the only molecular detuning reads $\Delta_- := \nu_2 - \nu$ ($\Delta_{21} = \Delta_{23}$), where ν_2 is the transition frequency of the 'middle' qubit. Here, for the ease of notation, the same symbol Δ_- as for the dimer case is used, but we should be aware that its definition is different. Due to the spatial symmetry of the trimer shown in Fig. 1, we also have $V_{12} = V_{23} \equiv V$, and $V > V_{13}$. Under this consideration, and without loss of generality, the effective three-qubit bare Hamiltonian can now be written as

$$H_{\rm trimer} = \begin{pmatrix} -\frac{3\nu_0}{2} & 0 & 0 & 0 & & 0 & 0 & 0 \\ 0 & -\frac{\nu_2}{2} & V & 0 & V_{13} & 0 & 0 & 0 \\ 0 & V & -\frac{\nu-\Delta_-}{2} & 0 & V & 0 & 0 & 0 \\ 0 & 0 & 0 & \frac{\nu_2}{2} & 0 & V & V_{13} & 0 \\ 0 & V_{13} & V & 0 & -\frac{\nu_2}{2} & 0 & 0 & 0 \\ 0 & 0 & 0 & V & 0 & \frac{\nu-\Delta_-}{2} & V & 0 \\ 0 & 0 & 0 & V_{13} & 0 & V & \frac{\nu_2}{2} & 0 \\ 0 & 0 & 0 & 0 & 0 & 0 & 0 & \frac{3\nu_0}{2} \end{pmatrix} \qquad (4)$$

where $\nu_0 = (\nu_1 + \nu_2 + \nu_3)/3 = (2\nu + \nu_2)/3$, and $\Delta_- = \nu_2 - \nu \ll \nu$. The dynamics of the trimer system is described by a master equation similar to that of Eq. (3), but replacing $\tilde{H}_{\rm dimer}$ by $H_{\rm trimer}$ (the total trimer Hamiltonian with the laser action is given in Appendix B), and by extending the incoherent sum term over indexes i,j from 1 to 3.

IV. PBI DIMER QUANTUM COHERENCE AND LOGIC GATING

For the dimer we next illustrate how one- and two-qubit logic gates, and hence entanglement and nonlocal correlations generation, is achieved. The dynamics of the dimer (two-qubit) system is described by means of the master equation (3), from which we obtain the density matrix and are able to simulate the physical realisation of logic gates as well as the generation of entanglement.

According to our description in the previous sections, the spontaneous emission rate (~ 200 MHz) of PBI is up to five orders of magnitude smaller than the electronic coupling V_{12} and the molecular detuning Δ_- (10^3 and 10^4 GHz, respectively). Since emission is the only dissipation channel, the dimer is a highly coherent quantum system. As we will show below, this means that coherent oscillations in the system's dynamics are about 1000 times faster than the spontaneous emission. We simulate several scenarios of coherent oscillation dynamics and show some striking results regarding the physical implementation of local as well as nonlocal gates useful for small-scale quantum computing based on the dimers.

A. Swap gate and natural entanglement

The dimer can 'naturally' generate the swap gate, which flips the two intermediate states of the 4-dimensional basis: $|01\rangle \rightarrow |10\rangle$, and vice versa. The matrix representation of the swap gate reads

$$U_{\rm swap} = \begin{pmatrix} 1 & 0 & 0 & 0 \\ 0 & 0 & 1 & 0 \\ 0 & 1 & 0 & 0 \\ 0 & 0 & 0 & 1 \end{pmatrix}. \qquad (5)$$

Figure 2 shows the pure generation of the swap gate

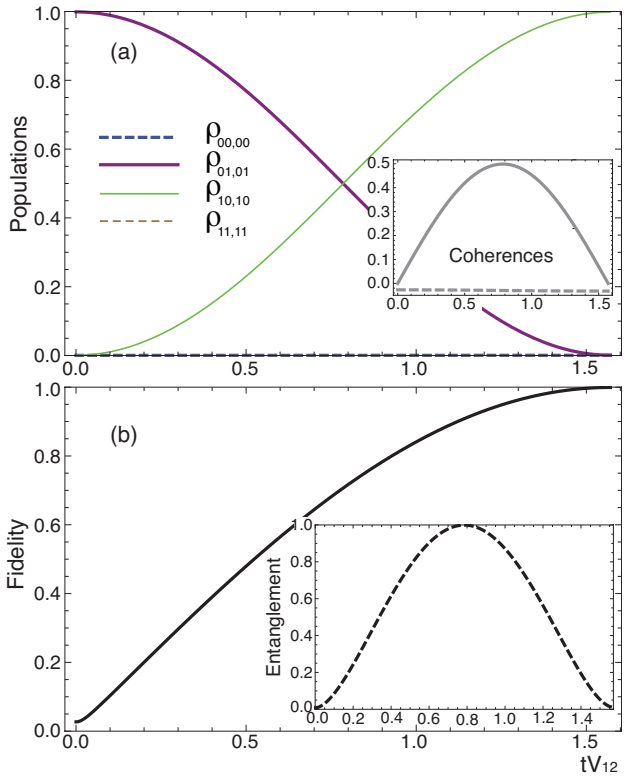

FIG. 2. Natural swap gate dynamics. (a) Populations $\rho_{01,01}$ (solid-purple) and $\rho_{10,10}$ (thin-solid-green). $\rho_{00,00}$ and $\rho_{11,11}$ are exactly zero. The inset shows $\mathcal{R}e\,[\rho_{01,10}]$ (dashed-gray) and $\mathcal{I}m\,[\rho_{01,10}]$ (solid-gray) of the relevant coherence. (b) Main: Fidelity of the swap gate; the time of the gate is $t_{\rm swap} = \pi/2V_{12}$. Inset: evolution of the EoF in the swap-gate process. $V_{12} = 1356$ GHz, $\Delta_- = 14.3$ GHz, $\Gamma = 172$ MHz, and $\Gamma_{12} = -86$ MHz. The time is given in units of V_{12}^{-1}.

for the situation $V_{12}/\Delta_- = 95 \gg 1$, see the caption for the detailed parameters. Note that the time axis has been plotted in V_{12}^{-1} units. From the ground $|00\rangle$ state, if we computationally flip qubit 2 to its excited state, the dimer is driven to the $|01\rangle$ state. Then, under the action of the electronic coupling V_{12}, after a time $t_{\rm swap} = \pi/(2V_{12}) \sim 1.2$ ps the dimer reaches the $|10\rangle$ state, as shown in the main graph of Fig. 2(a) where we plot the populations of this evolution, as well as the dynamics of the coherence $\rho_{01,10}$ (inset). Figure 2(b) gives the corresponding fidelity $\mathcal{F}(\rho,\sigma) = {\rm Tr}\left[\sqrt{\sqrt{\sigma}\rho\sqrt{\sigma}}\right]$, where σ is taken to be the expected state at the end of the gate and ρ is the evolving state of the dissipative dynamics. We find that the swap gate step has been carried out within ~ 1.2 ps with $\mathcal{F} = 1$. We remark that the swap gate operation continues (its dynamics exhibits coherent oscillations) for times up to two orders of magnitude longer than $t_{\rm swap}$. Intriguingly, the coherent oscillations lose only 5% of the maximum fidelity after around $t = 250 \times t_{\rm swap}$, i.e., for $t \approx 290$ ps (not shown).

One important byproduct of this conditional dynamics arises: By looking at the inset of Fig. 2(b), it is clear that the swap gate can be tailored to generate entanglement in the dimer. The entanglement is quantified by the entanglement of formation (EoF). For two-qubit systems, the EoF is analytically computed as $EoF(\rho) = h\left(\frac{1+\sqrt{1-C^2(\rho)}}{2}\right)$, where $h(x) = -x\log_2 x - (1-x)\log_2(1-x)$ is the binary entropy and $C(\rho) = \max\{0, \lambda_1 - \lambda_2 - \lambda_3 - \lambda_4\}$ is the so-called concurrence. λ_i's are the eigenvalues of the matrix $\sqrt{\rho(\sigma_y \otimes \sigma_y)\bar{\rho}(\sigma_y \otimes \sigma_y)}$, where $\bar{\rho}$ is the elementwise complex conjugate of ρ [28]. The maximal value of entanglement is reached at the time $t_{\rm swap}/2$. This simple scenario clearly shows the versatility of the dimer to generate single- as well as two-qubit quantum gates.

We next focus on the naturally-generated entanglement by means of the swap gate. In Fig. 3 we explicitly show the kind of entangled state that has been created for a ratio $V_{12}/\Delta_- = 0.5$. It is possible to generate the antisymmetric Bell state $|\Psi^-\rangle = \frac{1}{\sqrt{2}}(|01\rangle - |10\rangle)$ as shown by the populations (Fig. 3(a)) and coherences (Fig. 3(b)). The time required to obtain this entangled state, with a high fidelity (Fig. 3(c)), is $t_{\Psi^-} = \pi/2\sqrt{\Delta_-^2/4 + V_{12}^2} \sim 819$ fs, i.e., it is determined by the interplay between the molecular detuning and the electronic coupling. Such an entangled state is naturally robust to dissipation effects arising from the matrix host of the system and can be reached with fidelities around 95% for times longer than $1000 \times t_{\Psi^-}$. Figure 3(d) shows the population oscillations for a time $50 \times t_{\Psi^-}$. It is worth noting

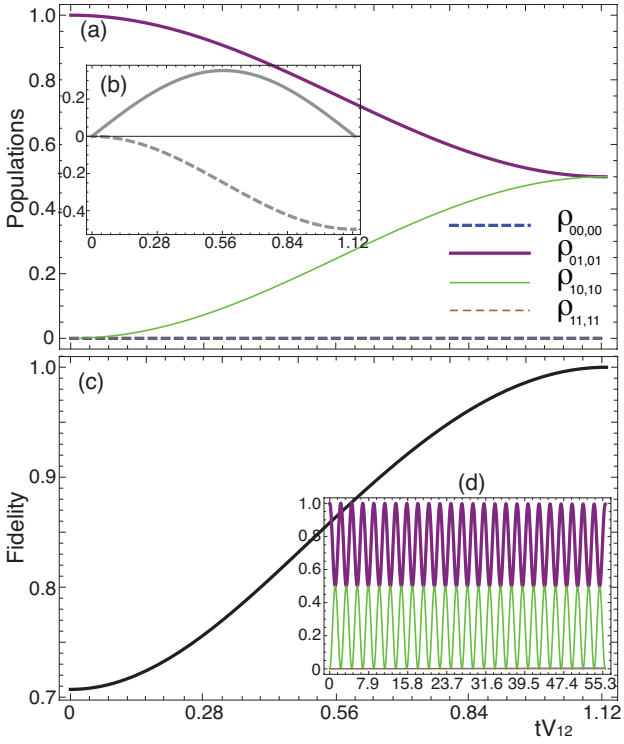

FIG. 3. Natural generation of the maximally entangled Bell state $|\Psi^-\rangle = \frac{1}{\sqrt{2}}(|01\rangle - |10\rangle)$, from the initial $|01\rangle$ state. (a) Populations, (b) coherence $\mathcal{R}e\,[\rho_{01,10}]$ (dashed) and $\mathcal{I}m\,[\rho_{01,10}]$ (solid), (c) fidelity with respect to the ideal Bell state, and (d) populations for $50 \times t_{\Psi^-}$. $\Delta_- = 190 \times 14.3$ GHz (see Fig. 2). Remaining parameters are as in Fig. 2.

that this entanglement dynamics is carried out with a molecular detuning two orders of magnitude higher than that used in Fig. 2, showing the large range with respect to the ratio V_{12}/Δ_- for which the PBI dimers are able to implement a conditional quantum dynamics and entanglement generation.

We emphasise that the swap gate cannot be implemented experimentally following the procedure outlined above. Owing to the optical diffraction limit of $\lambda_i/2 \sim 250$ nm, we cannot address single qubits within a dimer using an external laser. Only the entangled symmetric and antisymmetric Bell states $|\Psi^\pm\rangle = \frac{1}{\sqrt{2}}(|01\rangle \pm |10\rangle)$, two of the eigenstates of the dimer's Hamiltonian in Eq. (2), are optically accessible by a single-photon transition. Moreover, the doubly excited state $|11\rangle$ can be excited by a two-photon process [24]. Since these transitions into Bell states appear at different frequencies, the state to be excited can be selected by appropriately tuning the laser frequency. Alternatively, it can be easily shown from the molecular geometry (Fig. 1) that the symmetric and antisymmetric Bell states possess a mutually orthogonal transition dipole moment, i.e., selection is also possible using the laser polarisation. To generate an excitation localised on a single qubit of the dimer, and thus to realise the swap gate, a suitable coherent superposition of the Bell states $|\Psi^\pm\rangle$ is required, which can be achieved by an appropriate choice of the frequency bandwidth and/or polarisation of the laser. The subsequent dynamics within the system will then occur as outlined above. This *indirect* local action of the laser (or *computational* flipping) can be mathematically included in the model of Eq. (3) by assuming a local action of the laser Hamiltonian H_L. Finally, we note that in the molecular spectroscopy community the Bell states $|\Psi^\pm\rangle$ are known as Frenkel (or molecular) exciton states.

B. Generation of the full entangled Bell basis

We have shown that the PBI dimer can naturally generate the Bell states $|\Psi^\pm\rangle$ by means of their strongly coherent electronic coupling. As these two states are part of a complete 4-state orthonormal basis, the so-called Bell basis, they can be transformed, by computationally performing local operations, to the other two Bell states $|\Phi^\pm\rangle := \frac{1}{\sqrt{2}}(|00\rangle \pm |11\rangle)$. Appendix C shows an alternative scenario of dimer entanglement.

As shown in Fig. 4, the initial state $|\Psi^+\rangle$ is driven to the state $|\Phi'\rangle := \alpha\,|00\rangle + \beta\,|11\rangle$, with $\alpha \simeq 0.70$ and $\beta \simeq 0.57{+}0.42i$. This can be done by computationally flipping qubit 2. The remaining matrix elements are at least two orders of magnitude smaller. A similar result is obtained if we start from the state $|\Psi^-\rangle$, in which case we arrive at $|\Phi^*\rangle := -\beta^*\,|00\rangle + \alpha\,|11\rangle$ which in turn is orthogonal to the former one. This particular scenario has used the ideal $|\Psi^\pm\rangle$ states as our initial states: these can be prepared by following the recipe in Fig. 3 to entangle the monomers using the swap gate and then flipping the state of qubit 2. An alternative approach is illustrated in Fig. 8.

The set of required quantum operations to generate, for example, the $|\Phi^*\rangle$ state (up to a global phase) can be concatenated as $|\Phi^*\rangle \simeq \mathbb{1} \otimes \sigma_x\ U_{\rm swap}\ \mathbb{1} \otimes \sigma_x\,|00\rangle$. Although this three-gate circuit can be seen to be equivalent to the application of a local rotation on qubit 2 followed by a controlled-NOT ($U^{12}_{\rm CNOT}$) operation, we point out that the dimer reported here is not

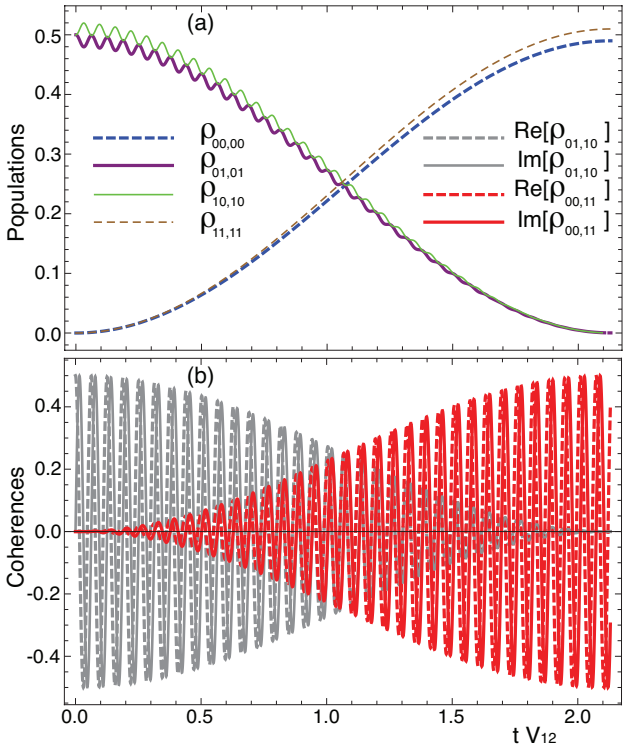

FIG. 4. (a) Populations and (b) coherences $\rho_{01,10}$ (gray) $\rho_{00,11}$ (red) in the generation of $\alpha\,|00\rangle + \beta\,|11\rangle$ states from the Bell $|\Psi^+\rangle$ state. Solid (dashed) stands for imaginary (real) part. The local action corresponds to flipping the state of qubit 2. Parameters as in Fig. 3.

able to directly simulate a controlled-NOT gate. This said, we have shown that these PBI dimers allow us to naturally simulate the non-local swap gate, which, in conjunction with single qubit operations, implement a universal gate set.

We have already mentioned above that the Bell states $|\Psi^{\pm}\rangle$ can be experimentally generated by laser excitation. The other two Bell states $|\Phi^{\pm}\rangle$ represent a superposition between the ground state and the two-photon accessible doubly excited state, which can also be induced by an external laser field.

V. PBI TRIMER ENTANGLEMENT AND NONLOCALITY

We quantify the dynamics of the zig-zag-type trimer system (see Fig. 1) by expanding the previous Hilbert space into the 2^3 dimensional space spanned by the computational basis states $|i\rangle\otimes|j\rangle\otimes|k\rangle$ $(i,j,k=0,1)$, taking into account all the cross-damping rates Γ_{ij}, and the coherent electronic couplings V_{ij}, which can be directly computed from Eqs. (A1) and (A2), by moving the subscripts $i,j=1,2,3$, and following a similar procedure to that for the dimer system.

In Eq. (4) we give the bare Hamiltonian (no laser) and in the Appendix B the full (laser-driven) Hamiltonian for the PBI trimer, as well as the distance-dependence of the collective effects. Diagonalisation of the Hamiltonian (4) leads to the identification of three classes of eigenstates: (i) two product states, (ii) two purely pairwise entangled states, and (iii) four possible tripartite entangled states, see Eq. (D1). An example of the latter class is the state:

$$|E_3\rangle = \frac{2V}{\sqrt{2\Delta^-(\Delta^- + V_{13} - \Delta_-)}}\big(\,|001\rangle + |100\rangle\,\big) - \sqrt{\frac{\Delta^- + V_{13} - \Delta_-}{2\Delta^-}}\,|010\rangle\,, \tag{6}$$

with eigenenergy $E_3 = -\frac{1}{2}(\nu - V_{13} + \Delta^-)$, where $\Delta^{\pm} = \sqrt{8V^2 + (V_{13} \pm \Delta_-)^2}$. $|E_3\rangle$ is a pairwise entangled state if $V/\Delta_- \ll 1$, but it exhibits genuine tripartite entanglement, otherwise. The exact form of the eight eigenstates and their respective PBI trimer eigenergies are left to the Appendix D.

We can excite different transitions between the eigenstates by applying an external coherent field. We begin by driving the transition $|E_1\rangle \leftrightarrow |E_3\rangle$ with a weak laser ($\Omega = 1$ GHz), and assume as initial state $|E_1\rangle \equiv |000\rangle$. We first assume as specific case a ratio $V/\Delta_- = 0.1$. Then the eigenstates are made up of pairwise entangled states and there are no tripartite entangled eigenstates. For instance, from Eq. (6) (see the numerics in Eq. (D2)), it is clear that the intermediate eigenstate $|E_3\rangle$ has only 1.9% of its population in the state $|010\rangle$, and almost all its population is in the superposition $0.70(|001\rangle + |100\rangle)$. This means that the three PBI monomers are not entangled at the same time, but just two of them exhibit entanglement and their state is separable with respect to the other monomer. Under these conditions the transition $|E_1\rangle \leftrightarrow |E_3\rangle$ occurs coherently as shown by the time evolution of the expectation values $\langle E_1|\,\rho(t)\,|E_1\rangle$ (blue) and $\langle E_3|\,\rho(t)\,|E_3\rangle$ (brown) in Fig. 5(a) and (c). The stationary state is a statistical mixture of the two involved states. A similar result is obtained when exciting the transition with a stronger laser amplitude $\Omega = 120$ GHz (inset of Fig. 5(b)).

The situation differs when assuming a ratio $V/\Delta_- = 1$ (Eq. (D3)). In this case, the four intermediate eigenstates are reasonable superpositions of three orthonormal states and they exhibit tripar-

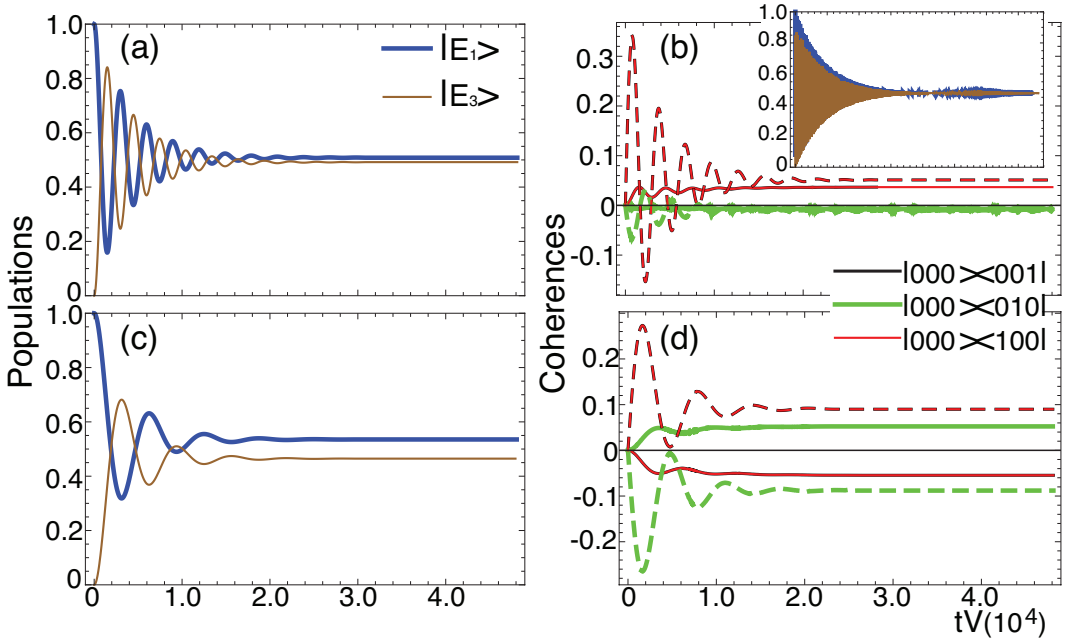

FIG. 5. Expectation values for the transition $|E_1\rangle \leftrightarrow |E_3\rangle$ under the action of a coherent (continuous) laser $\Omega = 1$ GHz. (a) Populations and (b) coherences (real (solid) and imaginary (dashed) part) with $\Delta_- = 12000$ GHz and $\nu_L = E_3 - E_1 = 700$ THz. (c) Populations and (d) coherences, $\Delta_- = 1200$ GHz and $\nu_L = E_3 - E_1 = 699$ THz. Real and imaginary curves for coherences $\rho_{000,001}$ (black) and $\rho_{000,100}$ (red) always take the same values, respectively. The inset shows the same populations as in (a) but with a laser amplitude $\Omega = 120$ GHz. Other used parameters are $V = 1200$ GHz, $V_{13} = -120$ GHz, $\Gamma = 172$ MHz, $\gamma_{12} = \gamma_{23} = -86$ MHz, and $\gamma_{13} = 172$ MHz.

tite entanglement (in fact, they all are W-like states). Such tripartite entanglement is present in the stationary regime being mixed with the ground state of the trimer (Fig. 5(c)) for the particular transition $|E_1\rangle \leftrightarrow |E_3\rangle$. The presence of some coherences at the end of the dynamics (more explicitly in Fig. 5(d)) implies that the stationary state is not completely classically correlated (a mixture of diagonal states) but still has quantum correlations assisted by the continuous action of the laser field.

A. Natural entanglement dynamics

Pairwise as well as W-like tripartite entangled states [29–31] are naturally generated as shown in Fig. 6 if we initiate the trimer computationally in the $|010\rangle$ state, i.e., the sandwiched monomer (qubit 2) is in the excited state and the other two in their ground state. Note that in an experiment this state can only be excited by creating a suitable coherent superposition of eigenstates (see Appendix D). After leaving the trimer to evolve exclusively by means of the electronic couplings, the system arrives to an almost perfect pairwise entangled state $1/\sqrt{2}(|100\rangle + |001\rangle) \equiv |\Psi^+\rangle_{13} \otimes |0\rangle_2$ (see vertical green line in Fig. 6). This corresponds to a maximally entangled state between qubits 1 and 3. Hence, the trimer state is separable with respect to the second qubit. This state is created after a time $t_{pw} = \pi/\sqrt{8V^2 + (V_{13} - \Delta_-)^2} \approx \pi/2\sqrt{2}V$, and such behaviour is expected according to the swapping effect due to V and the experimental criteria $V \gg V_{13} \geq \Delta_-$. The $\rho_{100,100}$ and $\rho_{001,001}$ curves superpose each other, as seen in Fig. 6(a), and the inset shows the coherent dynamics of populations for a time frame two orders of magnitude larger than that in the main plot.

Interestingly, this ultrafast dynamics allows the generation of tripartite entangled states as the so-called W-like states. Indeed, it is easy to show that under this evolution the only states propagating different from zero are those in the mixture $\rho_W(t) = p_1(t)\,|000\rangle\langle 000| + p_2(t)\,|W^*(t)\rangle\langle W^*(t)|$, where $|W^*(t)\rangle = a_1(t)\,|100\rangle + a_2(t)\,|010\rangle + a_3(t)\,|001\rangle$, $|a_1(t)|^2 + |a_2(t)|^2 + |a_3(t)|^2 = 1$, and $a_2(0) = 1$, are W-like states. Given the fact that $p_1(t) \ll p_2(t)$ for times shorter than the excited state lifetime, it follows that the states $\rho_W(t) \to |W^*(t)\rangle\langle W^*(t)|$ are basically

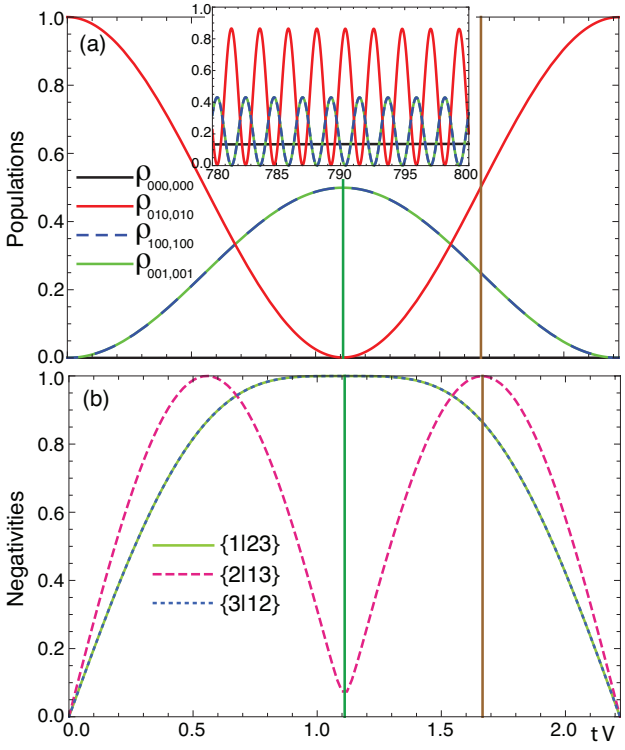

FIG. 6. Generation of pairwise (bipartite) entangled and tripartite W-like states via the monomers dipole-dipole couplings. (a) Main: Populations $\rho_{000,000}$ (black), $\rho_{010,010}$ (red), $\rho_{100,100}$ (blue) and $\rho_{001,001}$ (green). Inset: Same populations for $tV \in$ [780-800]. This is two orders of magnitude larger than the time in the main plot and one order of magnitude shorter than the relaxation time. Green vertical line at t_{pw} indicates the generation of a pairwise entangled state, and the brown line at $t_{\mathcal{W}} = 3t_{pw}/2$ highlights the generation of the $|\mathcal{W}\rangle$ state (see main text for full description). (b) Negativity with respect to the partition {1|23} (solid), {2|13} (dashed) and {3|12} (dotted). Parameters: $V = 1356$ GHz, $V_{13} = -122$ GHz ($|V_{13}| \sim 0.09\,V$), $\Gamma_{12} = \Gamma_{23} = -86$ MHz, $\Gamma_{13} = 172$ MHz, and $\Delta_- = 10$ GHz ($\sim 0.007\,V$), no laser. $\nu_2 > \nu_1 = \nu_3$ (similar results are obtained for different choice of frequencies–not shown).

the only ones present during the dynamics in this time frame.

The entanglement of this evolution has been quantified via the negativity [32] due to its operational interpretation and easiness of computation. For doing so, let us introduce $\{i|jk\}$ as a partition of the trimer system, where $i, j, k = 1, 2, 3$ stand for qubits $1, 2, 3$ respectively. Hence, negativity is computed on the three partitions $\{1|23\}$, $\{2|13\}$, and $\{3|12\}$ as plotted in Fig. 6(b). As expected, the negativities for $\{1|23\}$ and $\{3|12\}$ have the same behaviour due to the entanglement between qubits 1 and 3.

It is clear that the representative $|W\rangle = \frac{1}{\sqrt{3}}(|001\rangle + |010\rangle + |100\rangle)$ state belongs to the family of generated entangled $\rho_W(t)$ states. In Fig. 6(a) such state occurs at the intersection of the three corresponding populations. Another scenario explores a non-trivial behaviour of the negativity for the partition $\{2|13\}$: At its maximum value, marked by the brown line at $t_{\mathcal{W}} = (3/2)t_{pw}$ in Fig. 6, the trimer reaches the state

$$|\mathcal{W}\rangle = \frac{1}{2}\left(|100\rangle + \sqrt{2}e^{-\mathrm{i}0.489\pi}\,|010\rangle + |001\rangle\right). \quad (7)$$

This particular state is of great interest as it belongs to a subclass of W-like states that have been proven to be useful for teleportation and superdense coding [33].

B. PBI trimer nonlocal states

So far we have discussed (Sections IV and V A) the implementation of dimers and trimers based on PBI molecules as a valuable physical resource for quantum computing and information processing. We have also demonstrated conditional quantum dynamics and entanglement generation in dimers and trimers.

In this section, our concern is whether the entangled states are also nonlocal states. Nonlocality [29–31, 34] is a fundamental feature of quantum states that is not always equivalent to entanglement [29] and has been demonstrated to be useful for some tasks in information theory [30]. Nonlocality in bipartite states has been intensely studied and there are several different metrics for defining the nonlocality of quantum states, e.g., CHSH inequality, activation, and super activation of nonlocality, just to name a few [30, 35, 36]. For more than two qubits, however, the nonlocality formalism extends to 46 classes of inequalities; each of them gives a classical limit that could be exceeded by nonlocal quantum states [37]. Recently, analytical conditions to estimate the maximal violation of Mermin's inequality for three qubits were proposed [38, 39]. Furthermore, an interesting development on multipartite nonlocality with operational (experimental) interpretation and implementation, in terms of inequalities that just involve one- and two-body expectation values (up to two parties correlations), has been reported [40].

Some of the eigenstates of the trimer's Hamiltonian support entanglement. They can be directly excited

by a coherent laser and exhibit a robust dynamics against the slow dissipation due to spontaneous emission. The degree of entanglement, here caught by the Negativity (see Fig. 6(b)), depends on the interplay among the physical parameters; in particular, that between the molecular detuning and the effective electronic coupling.

In the context of quantum nonlocality, a nonlocal state is an entangled one [41], but the opposite does not always hold, and there are plenty of entangled but local states. As to the physical implementation of tripartite states, one question arises: are those trimer entangled states nonlocal? Here, we consider a Bell-like inequality and test it for some trimer entangled states: if such an inequality is violated hence the corresponding state is said to be nonlocal.

We numerically test Mermin's inequality [42] by considering that two dichotomic observables act on each PBI monomer, hence the inequality can be written as

$$\Upsilon \equiv \big|\langle A_1 B_2 B_3\rangle + \langle B_1 A_2 B_3\rangle + \langle B_1 B_2 A_3\rangle - \langle A_1 A_2 A_3\rangle\big| \leq 2, \tag{8}$$

which is the so-called $(3,2,2)$ scenario: three parties, two observables per party, and two outcomes per observable (dichotomic observables), and $\langle O\rangle = \mathrm{Tr}(\rho O)$ stands for the expectation value of the observable O. In our description of the PBI monomers as qubits, we write their associated observables in terms of the Pauli matrices $A_i = \cos\theta_i\sigma_z + \sin\theta_i\sigma_x$, and $B_i = \cos\phi_i\sigma_z + \sin\phi_i\sigma_x$, $i = 1,2,3$. Other observables in terms of combinations with σ_y can also be defined [43]. However, as the states explored in this section have a matrix structure with their anti-diagonal elements identically zero, observables in terms of σ_x plus σ_y do not exhibit any violation. Hence, the inequality (8) is evaluated in terms of the different angles θ_i, $\phi_i \in [-\pi,\pi]$, on the eigenstates supported by the trimer, and we search for at least one scenario in which Mermin's inequality (8) is violated.

The eigenstate $|E_3\rangle$ (see Eq. (6)) transforms into the W-like state $1/\sqrt{3}(|001\rangle - |010\rangle + |100\rangle)$ for the particular configuration $V = 1200\,\mathrm{GHz}$, $V_{13} = -120\,\mathrm{GHz}$, and $\Delta_- = 1080\,\mathrm{GHz}$. According to Mermin's inequality (8) this state is of course nonlocal with a maximum violation numerically found to be $\Upsilon \sim 3.05$.

We now look into the nonlocality of some of the states generated in the bare dynamics shown in Fig. 6. At $t = 0$, the initial (product) state $|010\rangle$ is of course local. However, at a later time, the pairwise entangled state reached at $t_{pw} \approx \pi/2\sqrt{2}V$ (green vertical line in Fig. 6) exhibits a maximum value $\Upsilon \sim 2.8$. In a similar way, the W-like state Eq. (7) reached at $t_{\mathcal{W}} \approx 3\pi/4\sqrt{2}V$ (brown vertical line in Fig. 6) also violates Mermin's inequality as the function Υ attains a maximum of ~ 2.2. We then conclude that these two states naturally generated by the trimer are both nonlocal states in the sense of the $(3,2,2)$ scenario. It is worth noting that the above two states are not pure at all because, in both cases, there exists a contribution due to the ground $|000\rangle$ state, as expected. Then, they both can be written as $(1-p)|000\rangle\langle 000| + p|\Psi_{pw}\rangle\langle\Psi_{pw}|$ and $(1-p)|000\rangle\langle 000| + p|\mathcal{W}\rangle\langle\mathcal{W}|$, respectively. We have identified $|\Psi_{pw}\rangle \equiv |\Psi^+\rangle_{13} \otimes |0\rangle_2$. Despite this fact, and thanks to the slow spontaneous emission of the trimer, the contribution of the ground state is up to three orders of magnitude smaller than the contribution of the relevant states. As a consequence, the maximum values obtained for the violation of the Mermin's inequality agree with the maximal violation of the corresponding pure state ($p = 1$ in both cases). This behaviour persists up to hundreds of picoseconds as it is shown for the bare dynamics in the inset of Fig. 6(a).

VI. SUMMARY

For the implementation of quantum logic gating, entanglement, and nonlocality in nanostructures based on organic molecules, we have considered here, without loss of generality, the particular arrangement shown in Fig. 1. The transition dipole moments of the PBI molecules in the dimer and trimer span one plane and possess an opening angle $\theta = 120°$. However, as mentioned above, the separation between the molecules (i.e. transition dipole moments) as well as their mutual orientation can be tailored by chemical synthesis. Hence, the values for the collective damping (A1) and electronic couplings between transition dipole moments (A2) can be tuned in this way. For instance, the molecules could be arranged such that their transition dipole moments are parallel to each other; this would result in a smaller nearest-neighbour distance, thus in a stronger electronic coupling and as a consequence in a higher degree of entanglement between them.

For the dimer, we have shown how to drive a condi-

tional quantum dynamics to achieve one-qubit (one-PBI-monomer) and two-qubit gates. We also demonstrated that all the entangled Bell basis states can be experimentally implemented in the dimer.

In the trimer analysis we have additionally tested the nonlocality of the naturally generated entangled states. We have numerically shown that a W-like state can be exactly obtained for specific combinations of the coherent electronic couplings and the molecular detuning. Furthermore, we also computed the corresponding locality violation for the dynamically generated pairwise ($|\Psi_{pw}\rangle$) and W-like ($|\mathcal{W}\rangle$) states (see Fig. 6).

Our results on entanglement generation in both dimers and trimers reveal that the dynamics in these systems is highly coherent on the sub-picosecond and picosecond time scales; the relaxation time of their excited states lies in the nanosecond scale. This means that quantum gate operations with a high fidelity (coherent operations) are carried out in the sub-picoseconds scale (10^4-10^5 times faster than their life time).

Our study can also be extended to many-body systems because organic molecules can be synthesised to self-assemble into micrometre-long, fibrillar structures containing up to 10^4 molecules [1]. The very dense packing of molecules in such systems results in strong electronic coupling between their transition dipole moments and thus should allow for the formation of entangled states on a macroscopic scale.

ACKNOWLEDGEMENTS

J.H.R. and C.E.S acknowledge support by the Colombian Science, Technology and Innovation Fund-General Royalties System (Fondo CTeI-Sistema General de Regalías) under contract BPIN 2013000100007, Universidad del Valle for partial funding (grant CI 7930), and Colciencias (grant CI 71003). We gratefully acknowledge Andrés Ducuara for fruitful discussions. C.E.S. thanks Colciencias for a Fellowship and Universidad de Córdoba (grant CA-097). R.H. acknowledges support from the Elite Network of Bavaria (ENB, *Macromolecular Science*) and from the German Research Foundation (DFG) through project HI1508/3.

Appendix A: General expressions for the PBI collective damping and the dipole-dipole coupling

The coherent coupling V_{ij}, and the cross-damping rate Γ_{ij} for a sample of N qubits are computed, respectively, as [27]:

$$\Gamma_{ij} = \frac{3}{2}\sqrt{\Gamma_i\Gamma_j}\Big\{ [\hat{\boldsymbol{\mu}}_i\cdot\hat{\boldsymbol{\mu}}_j - (\hat{\boldsymbol{\mu}}_i\cdot\hat{\mathbf{r}}_{ij})(\hat{\boldsymbol{\mu}}_j\cdot\hat{\mathbf{r}}_{ij})]\,\frac{\sin z_{ij}}{z_{ij}} + [\hat{\boldsymbol{\mu}}_i\cdot\hat{\boldsymbol{\mu}}_j - 3(\hat{\boldsymbol{\mu}}_i\cdot\hat{\mathbf{r}}_{ij})(\hat{\boldsymbol{\mu}}_j\cdot\hat{\mathbf{r}}_{ij})]\Big(\frac{\cos z_{ij}}{z_{ij}^2} - \frac{\sin z_{ij}}{z_{ij}^3}\Big)\Big\}, \tag{A1}$$

$$V_{ij} = \frac{3}{4}\sqrt{\Gamma_i\Gamma_j}\Big\{ [(\hat{\boldsymbol{\mu}}_i\cdot\hat{\mathbf{r}}_{ij})(\hat{\boldsymbol{\mu}}_j\cdot\hat{\mathbf{r}}_{ij}) - \hat{\boldsymbol{\mu}}_i\cdot\hat{\boldsymbol{\mu}}_j]\,\frac{\cos z_{ij}}{z_{ij}} + [\hat{\boldsymbol{\mu}}_i\cdot\hat{\boldsymbol{\mu}}_j - 3(\hat{\boldsymbol{\mu}}_i\cdot\hat{\mathbf{r}}_{ij})(\hat{\boldsymbol{\mu}}_j\cdot\hat{\mathbf{r}}_{ij})]\Big(\frac{\cos z_{ij}}{z_{ij}^3} + \frac{\sin z_{ij}}{z_{ij}^2}\Big)\Big\}, \tag{A2}$$

where $z_{ij} = nk_{ij}r_{ij}$, n denotes the matrix refractive index, $k_{ij} = \omega_{ij}/c$, and $\omega_{ij} = \pi(\nu_i + \nu_j)$. $\boldsymbol{\mu}_i$ is the dipole transition moment and $\boldsymbol{r}_{ij}$ is the separation vector between the centres of the two monomers i and j; $i, j = 1, ..., N$. Under the rotating wave approximation-RWA, we can simplify the notation to $\omega_{ij} \to 2\pi\nu_0$ as the inequality $|\nu_i - \nu_j| \ll \nu_0$ holds for all pairs of subscripts ij.

Appendix B: PBI Trimer Hamiltonian

The driven Hamiltonian for the three-qubit system is straightforwardly extended from Eq. (2). Considering the fixed coplanar configuration shown in Fig. 1 for the trimer, the Hamiltonian reads:

$$\tilde{H}_{\text{trimer}} = \frac{1}{2}\begin{pmatrix} -\delta_1 & \Omega & \Omega & 0 & \Omega & 0 & 0 & 0 \\ \Omega & -\delta_2 & 2V_{23} & \Omega & 2V_{13} & \Omega & 0 & 0 \\ \Omega & 2V_{23} & -\delta_3 & \Omega & 2V_{12} & 0 & \Omega & 0 \\ 0 & \Omega & \Omega & \delta_2 & 0 & 2V_{12} & 2V_{13} & \Omega \\ \Omega & 2V_{13} & 2V_{12} & 0 & -\delta_2 & \Omega & \Omega & 0 \\ 0 & \Omega & 0 & 2V_{12} & \Omega & \delta_3 & 2V_{23} & \Omega \\ 0 & 0 & \Omega & 2V_{13} & \Omega & 2V_{23} & \delta_2 & \Omega \\ 0 & 0 & 0 & \Omega & 0 & \Omega & \Omega & \delta_1 \end{pmatrix}, \tag{B1}$$

where $\delta_1 = 3(\nu_0 - \nu_L)$, $\delta_2 = \nu_2 - \nu_L$, $\delta_3 = \nu - \Delta_- - \nu_L$. Given the planar structure of the trimer (see Fig. 1), we estimate the following values for the collective parameters; $V_{12} = V_{23} \approx 1356$ GHz, $\Gamma_{12} = \Gamma_{23} \approx -86$ MHz (the separation between monomers 1-2 and 2-3 is 2.2 nm). For monomers 1 and 3 we have $V_{13} \approx -122$ GHz and $\Gamma_{13} \approx 172$ MHz as their separation is 4.4 nm. For the specific computation of

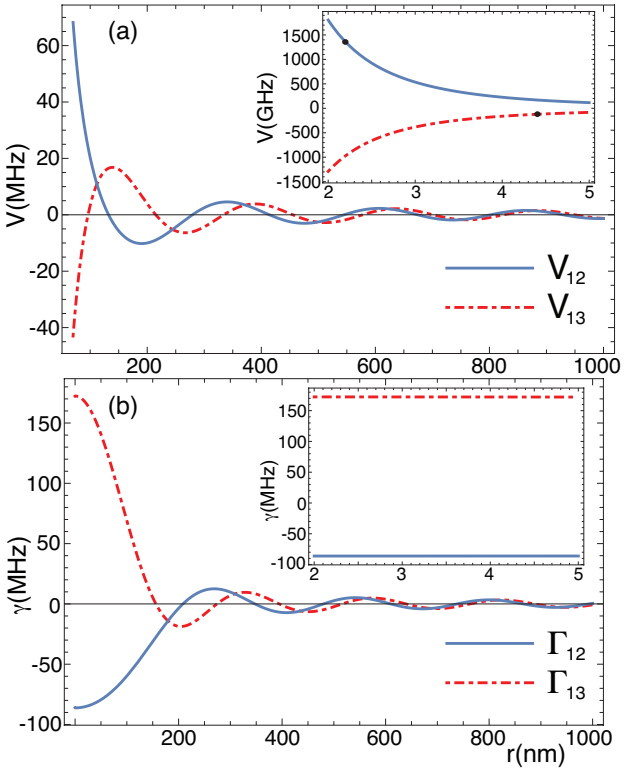

FIG. 7. (a) Dipole-dipole couplings V_{12} (solid) and V_{13} (dashed), (b) collective damping Γ_{12} (solid) and Γ_{13} (dashed). The two black dots in the inset of (a) show the specific inter-qubit separation for the computed values in the main text.

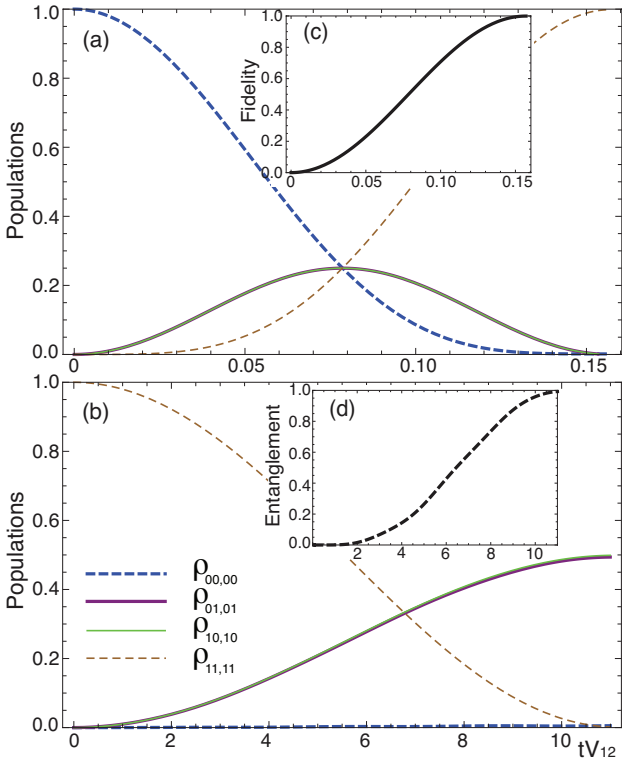

FIG. 8. Entanglement from the doubly-excited state. (a) Transition from the ground $|00\rangle$ (dashed-blue) to the doubly-excited $|11\rangle$ (thin-dashed-brown) state. $\Delta_+ = 0$ and $\Omega = 27116$ GHz. (b) Driven dynamics from the $|11\rangle$ state to the maximally entangled $|\Psi^+\rangle$ state. $\Omega/2 = 135.6$ GHz, and $\Delta_+ = 2\sqrt{(\Delta_-/2)^2 + V_{12}^2}$. (c) Fidelity evolution of the $|00\rangle \rightarrow |11\rangle$ transition. (d) EoF generated during this process. Γ, Γ_{12} and V_{12} as in Fig. 2, and the molecular detuning $\Delta_- = 0.01V$ (13.6 GHz).

these values from the general expressions Eqs. (A1) and (A2), we have considered the dipole moments associated to qubits 1 and 3 to be parallel to each other, thus the closer dimers exhibit a repulsive interaction and the farthest ones an attractive one.

Figure 7 shows the general behaviour of the collective parameters in the trimer system: (a) shows the behaviour of V_{12} (solid curve) and V_{13} (dashed curve) as functions of the mutual separation $\boldsymbol{r}$ from 70 nm to 1000 nm. The inset shows a zoom of such separation in the region [2-5] nm. The inter-monomer separation for which the above numerical values were computed are represented by the two black dots in the inset of (a). The corresponding behaviour of Γ_{12} and Γ_{13} is shown in (b).

The time evolution of the trimer density matrix elements are numerically computed by extending the master equation Eq. (3) to the new Hamiltonian Eq. (B1), and by adding Γ_3 and Γ_{13} terms to the Lindblad operator.

Appendix C: Laser-induced entanglement through doubly excited state

As an alternative of the natural entanglement generation shown in Section IV A, in this appendix we give another scenario in which the entangled $|\Psi^{\pm}\rangle$ states can be excited by means of a two-photon process. The dimer is driven to the doubly-excited $|11\rangle$ state within a time π/Ω ($\Omega \approx 27116$ GHz), as shown in Fig. 8(a). This strong laser strength ($\Omega/2 = 10V_{12}$) is required as the energy difference between these two states is $\nu_1 + \nu_2$. This transition occurs with high fidelity in ~ 116 fs (Fig. 8(c)). After this step, the Bell state $|\Psi^+\rangle$ can be excited by setting the coherent laser to $\Omega/2 = 0.1V_{12}$ ($\Omega \approx 271$ GHz), and applying it for a time $t_{\Psi^+} \simeq 7\pi/10\Omega$ or, equivalently, for $t_{\Psi^+} \simeq 7\pi/2V_{12}$. This time roughly corresponds to $t_{\Psi^+} \sim 8.1$ ps (Fig. 8(b)), and the total process time is

~ 8.2 ps. Figure 8(d) shows the EoF for the second step.

In spite of the fact that the identical-molecule scenario ($\Delta_- = 0$) would be a desired one, we have tested the more realistic case of detuned molecules. In doing so, we considered $\Delta_- = 0.01V_{12}$ (13.6 GHz) in Fig. 8; however, we point out that this entanglement generation also works for $\Delta_- = 0.1V_{12}$, and even for $\Delta_- = V_{12}$ (1356 GHz): in this latter case the maximum value for the EoF is ~ 0.85. The interplay between the molecular detuning and the electronic interaction is also evident as the laser detuning must satisfy $\Delta_+ = 2\sqrt{(\Delta_-/2)^2 + V_{12}^2}$ for this population transition to occur. If instead, we excite with a perfect resonance ($\Delta_+ = 0$), the ground state will increase quickly and an entangled state like that shown in Fig. 8(b) will never appear. Additional to this resonance condition, a trade-off between the laser and the electronic interaction strengths is also a crucial factor for producing the entanglement evolution of Fig. 8(b) as they must satisfy $\Omega < V_{12}$. For laser strengths of the same order of or higher than V_{12}, the entangling effect is washed away.

We emphasise that the PBI coherent dynamics persists up to hundreds of picoseconds. For the case of Fig. 8(b), the total mixed state is $(1-p(t))\,|11\rangle\langle 11| + p(t)\,|\Psi^+\rangle\langle\Psi^+|$, where the time evolution might be captured in the parameter $p(t)$, with $p(0) = 0$, and hence for $t_m = mt_{\Psi^+} \equiv m(7\pi/2V_{12})$; $m = 1, 2, 3, ...$, we have $p(t_m) = 1$, and thus the entangled $|\Psi^+\rangle$ state.

Appendix D: PBI Trimer eigensystem

The eight eigenstates of the bare trimer Hamiltonian (4) with their respective eigenenergies can be analytically computed and read

$$
\begin{aligned}
&E_1 = -\frac{3}{2}\nu_0;\ |E_1\rangle = |000\rangle\,;\ \ E_2 = -(\nu_2/2 + V_{13});\ |E_2\rangle = \frac{1}{\sqrt{2}}(-|001\rangle + |100\rangle);\\
&E_3 = -\frac{1}{2}(\nu - V_{13} + \Delta^-);\ |E_3\rangle = \frac{2V}{\sqrt{2\Delta^-(\Delta^- + V_{13} - \Delta_-)}}(|001\rangle + |100\rangle) - \sqrt{\frac{\Delta^- + V_{13} - \Delta_-}{2\Delta^-}}\,|010\rangle\,;\\
&E_4 = -\frac{1}{2}(\nu - V_{13} - \Delta^-);\ |E_4\rangle = \frac{2V}{\sqrt{2\Delta^-(\Delta^- - V_{13} + \Delta_-)}}(|001\rangle + |100\rangle) + \sqrt{\frac{\Delta^- - V_{13} + \Delta_-}{2\Delta^-}}\,|010\rangle\,;\\
&E_5 = \frac{1}{2}(\nu + V_{13} - \Delta^+);\ |E_5\rangle = \frac{2V}{\sqrt{2\Delta^+(\Delta^+ + V_{13} + \Delta_-)}}(|011\rangle + |110\rangle) - \sqrt{\frac{\Delta^+ + V_{13} + \Delta_-}{2\Delta^+}}\,|101\rangle\,;\\
&E_6 = \frac{1}{2}(\nu + V_{13} + \Delta^+);\ |E_6\rangle = \frac{2V}{\sqrt{2\Delta^+(\Delta^+ - V_{13} - \Delta_-)}}(|011\rangle + |110\rangle) + \sqrt{\frac{\Delta^+ - V_{13} - \Delta_-}{2\Delta^+}}\,|101\rangle\,;\\
&E_7 = \nu_2/2 - V_{13};\ |E_7\rangle = \frac{1}{\sqrt{2}}(-|011\rangle + |110\rangle);\ \ E_8 = \frac{3}{2}\nu_0;\ |E_8\rangle = |111\rangle\,,
\end{aligned}
\tag{D1}
$$

where $\Delta^\pm = \sqrt{8V^2 + (V_{13} \pm \Delta_-)^2}$. To estimate the magnitude of the eigenenergies and the eigenstates coefficients, we choose the following parameters: $V/\Delta_- = 0.1$; $V = 1200$ GHz, $V_{13} = -120$ GHz, $\Delta_- = 12000$ GHz, $\nu = 700$ THz and $\nu_2 = 712$ THz ($\Delta_-/\nu_0 \simeq 0.02$). Thus, the eigensystem now reads

$$
\begin{aligned}
&E_1 = -1056\,\text{THz};\ |E_1\rangle = |000\rangle\,;\ \ E_2 = -355.9\,\text{THz};\ |E_2\rangle = \frac{1}{\sqrt{2}}(-|001\rangle + |100\rangle);\\
&E_3 = -356.3\,\text{THz};\ |E_3\rangle = 0.7005(|001\rangle + |100\rangle) - 0.1361\,|010\rangle\,;\\
&E_4 = -343.8\,\text{THz};\ |E_4\rangle = 0.0962(|001\rangle + |100\rangle) + 0.9907\,|010\rangle\,;\\
&E_5 = 343.8\,\text{THz};\ |E_5\rangle = 0.0981(|011\rangle + |110\rangle) - 0.9903\,|101\rangle\,;\\
&E_6 = 356.1\,\text{THz};\ |E_6\rangle = 0.7003(|011\rangle + |110\rangle) + 0.1387\,|101\rangle\,;\\
&E_7 = 356.1\,\text{THz};\ |E_7\rangle = \frac{1}{\sqrt{2}}(-|011\rangle + |110\rangle);\ \ E_8 = 1056\,\text{THz};\ |E_8\rangle = |111\rangle\,.
\end{aligned}
\tag{D2}
$$

For a smaller molecular detuning such that $V/\Delta_- = 1$; $\Delta_- = 1200$ GHz and $\nu_2 = 701$ THz,

the eigensystem becomes

$$
\begin{aligned}
&E_1 = -1050.6\,\mathrm{THz};\ |E_1\rangle = |000\rangle\,;\quad E_2 = -350.5\,\mathrm{THz};\ |E_2\rangle = \frac{1}{\sqrt{2}}(-|001\rangle + |100\rangle);\\
&E_3 = -351.9\,\mathrm{THz};\ |E_3\rangle = 0.5836(|001\rangle + |100\rangle) - 0.5646\,|010\rangle\,;\\
&E_4 = -348.2\,\mathrm{THz};\ |E_4\rangle = 0.3992(|001\rangle + |100\rangle) + 0.8254\,|010\rangle\,;\\
&E_5 = 348.2\,\mathrm{THz};\ |E_5\rangle = 0.4174(|011\rangle + |110\rangle) - 0.8072\,|101\rangle\,;\\
&E_6 = 351.7\,\mathrm{THz};\ |E_6\rangle = 0.5708(|011\rangle + |110\rangle) + 0.5902\,|101\rangle\,;\\
&E_7 = 350.7\,\mathrm{THz};\ |E_7\rangle = \frac{1}{\sqrt{2}}(-|011\rangle + |110\rangle);\quad E_8 = 1050.6\,\mathrm{THz};\ |E_8\rangle = |111\rangle\,. \qquad \text{(D3)}
\end{aligned}
$$

As explained in the main text, the scenario given by Eq. (D2) clearly shows that non tripartite entangled states are generated. Hence, only pairwise and product states build up the eigensystem. On the other hand, in the second scenario we can see that the states from $|E_3\rangle$ to $|E_6\rangle$ are superpositions with significant contributions around the three compounding states, thus being genuine tripartite entangled states.

BIBLIOGRAPHY

[1] A. T. Haedler, *et al.*, Nature, **523**, 196-199 (2015).

[2] G. D. Scholes, *et al.*, Nature **543**, 647-656, (2017).

[3] C. A. Melo-Luna, *et al.*, Scientific Reports **7**, 44730 (2017).

[4] J-L. Bredas, E. H. Sargent and G. D. Scholes, Nature Materials **16**, 35 (2017).

[5] J. Eckel, J. H. Reina and M. Thorwart, New Journal of Physics **11**, 085001 (2009).

[6] A. Streltsov, G. Adesso, and M. B. Plenio, Rev. Mod. Phys. **89**, 041003 (2017).

[7] M. Thorwart, J. Eckel, J. H. Reina, P. Nalbach and S. Weiss, Chemical Physics Letters **478**, 234 - 237 (2009).

[8] T. Basché, W. E. Moerner, M. Orrit and U. P. Wild, 2007, *Single-Molecule Optical Detection, Imaging and Spectroscopy*, VCH Verlagsgesellschaft mbH.

[9] A. Weigel, A. Sebesta and P. Kukura, J. Phys. Chem. Lett. **6**, 4032-4037 (2015).

[10] D. Brinks, *et al.*, Chem. Soc. Rev. **43**, 2476-2491 (2014).

[11] N. Accanto, *et al.*, Light Sci. Appl. **6**, e16239 (2016).

[12] R. Hildner, D. Brinks and N. F. van Hulst, Nature Physics **7**, 172-177 (2011).

[13] E. Romero, V. I. Novoderezhkin and R. van Grondelle, Nature **543**, 355 (2017).

[14] G. D. Scholes, G. R. Fleming, A. Olaya-Castro and R. van Grondelle, Nature Chemistry **3**, 763-774 (2011).

[15] S.F. Huelga and M.B. Plenio, Contemporary Physics **54**, 181-207 (2013).

[16] R. J. Cogdell, A. Gall and J. Köhler, Quarterly Reviews of Biophysics **39**, 227-324 (2006).

[17] A. Issac, R. Hildner, C. Hippius, F. Würthner and J. Köhler, ACS Nano **8**, 1708 (2014).

[18] A. Polman, M. Knight, E. C. Garnett, B. Ehrler and W. C. Sinke, Science **352**, 6283 (2016).

[19] E. Lang, *et al.*, Chem. Phys. Chem. **8**, 1487-1496 (2007).

[20] A. Issac, *et al.*, Phys. Chem. Chem. Phys. **14**, 10789-10798 (2012).

[21] D. Ernst, R. Hildner, C. Hippius, F. Würthner and J. Köhler, Chem. Phys. Lett. **482**, 93-98 (2009).

[22] J. H. Reina, R. G. Beausoleil, T. P. Spiller and W. J. Munro, Phys. Rev. Lett. **93**, 250501 (2004).

[23] C. E. Susa and J. H. Reina, Phys. Rev. A **85**, 022111 (2012).

[24] C. Hettich, *et al.*, Science **298**, 385-389 (2002).

[25] C. E. Susa and J. H. Reina, Phys. Rev. A **82**, 042102 (2010).

[26] J. H. Reina, C. E. Susa and F. F. Fanchini, Scientific Reports **4**, 7443 (2014).

[27] Z. Ficek and S. Swain, 2005, *Quantum Interference and Coherence: Theory and Experiments*, Springer-Verlag New York.

[28] W. K. Wootters, Phys. Rev. Lett. **80**, 2245 (1998).

[29] R. Augusiak, M. Demianowicz and A. Acín, J. Phys. A **47**, 424002 (2014).

[30] D. Cavalcanti, A. Acín, N. Brunner and T. Vértesi, Phys. Rev. A **87**, 042104 (2013).

[31] A. F. Ducuara, J. Madroñero and J. H. Reina, Universitas Scientiarum **21**, 129-158 (2016).

[32] G. Vidal and R. F. Werner, Phys. Rev. A **65**, 032314 (2002).

[33] P. Agrawal and A. Pati, Phys. Rev. A **74**, 062320 (2006).

[34] A. F. Ducuara, C. E. Susa and J. H. Reina, J. Phys. A **50**, 265302 (2017).

[35] M. Navascués and T. Vértesi, Phys. Rev. Lett. **106**, 060403 (2011).
[36] C. Palazuelos, Phys. Rev. Lett. **109**, 190401 (2012).
[37] C. Śliwa, Phys. Lett. A **317**, 165-168 (2003).
[38] B. Paul, K. Mukherjee and D. Sarkar, Phys. Rev. A **94**, 032101 (2016).
[39] S. Adhikari and A. S. Majumdar, arXiv:1602.02619v1 (2016).
[40] J. Tura, *et al.*, Science **344**, 1256-1258 (2014).
[41] J-L. Chen, C. F. Wu, L. C. Kwek and C. H. Oh, Phys. Rev. Lett. **93**, 140407 (2004).
[42] N. D. Mermin, Phys. Rev. Lett. **65**, 1838 (1990).
[43] J. Chang and Y. Kwon, Chaos, Solitons & Fractals **41**, 1201-1207 (2009).